RESEARCH ARTICLE

Key Points:
- Reappraisal of maximum cross correlation using high spatial and temporal resolution data
- Blue and green water-leaving radiance give similar results to chlorophyll product
- Accuracy of derived currents relative to HF radar $\sim$20 cm/s

Correspondence to:
M. A. Warren,
mark1@pml.ac.uk

Estimation of ocean surface currents from maximum cross correlation applied to GOCI geostationary satellite remote sensing data over the Tsushima (Korea) Straits

M. A. Warren[1], G. D. Quartly[1], J. D. Shutler[2], P. I. Miller[1], and Y. Yoshikawa[3,4]

[1]Plymouth Marine Laboratory, Plymouth, UK, [2]Center for Geography, Environment and Society, University of Exeter, Penryn, UK, [3]Research Institute for Applied Mechanics, Kyushu University, Kyushu, Japan, [4]Now at Graduate School of Science, Kyoto University, Kyoto, Japan

Abstract Attempts to automatically estimate surface current velocities from satellite-derived thermal or visible imagery face the limitations of data occlusion due to cloud cover, the complex evolution of features and the degradation of their surface signature. The Geostationary Ocean Color Imager (GOCI) provides a chance to reappraise such techniques due to its multiyear record of hourly high-resolution visible spectrum data. Here we present the results of applying a Maximum Cross Correlation (MCC) technique to GOCI data. Using a combination of simulated and real data we derive suitable processing parameters and examine the robustness of different satellite products, those being water-leaving radiance and chlorophyll concentration. These estimates of surface currents are evaluated using High Frequency (HF) radar systems located in the Tsushima (Korea) Strait. We show the performance of the MCC approach varies depending on the amount of missing data and the presence of strong optical contrasts. Using simulated data it was found that patchy cloud cover occupying 25% of the image pair reduces the number of vectors by 20% compared to using perfect images. Root mean square errors between the MCC and HF radar velocities are of the order of 20 cm s^{-1}. Performance varies depending on the wavelength of the data with the blue-green products out-performing the red and near infra-red products. Application of MCC to GOCI chlorophyll data results in similar performance to radiances in the blue-green bands. The technique has been demonstrated using specific examples of an eddy feature and tidal induced features in the region.

1. Introduction

Ocean currents dictate the movement of water around the globe, transporting and mixing nutrients, salts, gases, biology and heat throughout the oceans. This means that knowledge about the existence of currents, their directions and speed of flow are important to many commercial, societal and research sectors and services. For example, industries such as oil and gas exploration require reliable data about the existence and strength of currents that are local to their installations, to ensure safe working conditions and to understand the stresses that the installations are exposed to [*Crout*, 2008]. Also, ships and recreational vessels rely on ocean current information for route planning to minimize fuel use [*Ronen*, 2011] or to gain a tactical advantage over rivals in a race. Other applications include maritime search and rescue, water pollution mapping and containment, larval transport and global heat transport [*Klemas*, 2012].

Methods for quantitatively observing or estimating current information fall into two broad observation categories: in situ or remote sensing. In situ observations are typically spatially sparse data sets that take a point measurement at intervals e.g., via moorings, buoys or on a ship. Whereas remote sensing observations (i.e., sensing or observing from a distance) include shore-based techniques and airborne- or satellite-based techniques that employ active or passive systems such as high frequency (HF) radar, altimetry, synthetic aperture radar or radiometry [*Shutler et al.*, 2016]. The spatial scale for remote sensing methods is typically either dense regional observations or sparse global observations, which are integrated in some sense over a resolution cell with a spatial resolution of the order of 1 m to multiple kilometers. These spatial and temporal scales vary dependent upon the type of sensors employed, network density or orbit (flight path) of the satellite (aircraft). However, due the high spatial coverage and short acquisition times of remote sensing instruments, this method is well placed to monitor large areas such as the oceans.
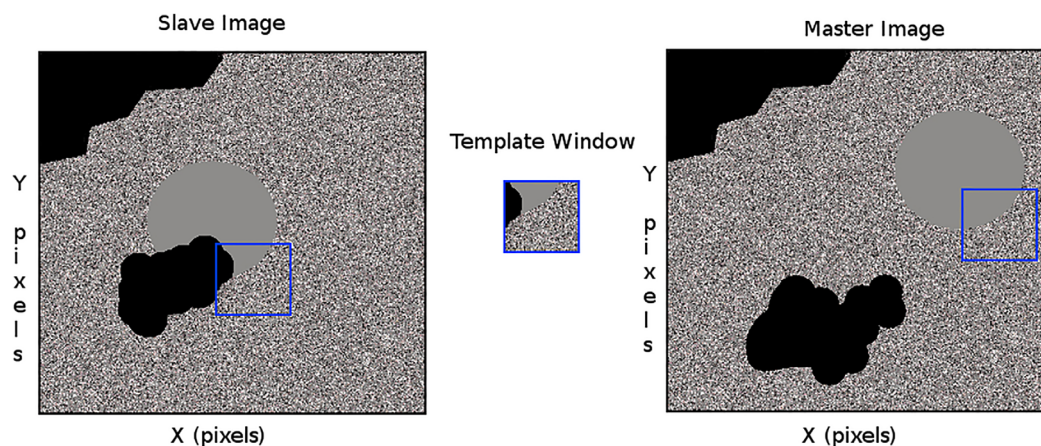
Figure 1. Illustration of the MCC technique applied to simple synthetic data sets of a solid disc of increased numerical value. The template region is a section from the slave image as shown by the box. The template region is matched against every possible position in the master image. The position that provides the best match (shown as the box in the master image) is identified from the maximum cross correlation of each position. For identifying ocean currents, the method must ignore any cloud and land masked pixels (shown here in black).

One scientifically mature technique that has previously been used to determine ocean current data from satellite remote sensing observations is the maximum cross correlation (MCC) and its variants. Strictly speaking, this approach allows the ocean surface velocity to be derived. In essence, the method compares temporally separated data fields (images) derived from satellite observations (e.g., sea-surface temperature (SST) or chlorophyll) in an attempt to follow the movement of characteristic features by finding parts of one image that closely match a succeeding image (see Figure 1). A velocity is inferred for that patch of water by dividing the displacement vector by the known time interval between images. *Emery et al.* [1986], *Tokmakian et al*. [1990], *Bowen et al*. [2002], and others have shown in previous work that it is possible to use MCC techniques to retrieve ocean surface velocities from Advanced Very High Resolution Radiometer (AVHRR) infra-red and Coastal Zone Color Scanner (CZCS) ocean color satellite image pairs separated by 6–24 h. In more recent work, *Crocker et al*. [2007] have derived ocean current measurements using an MCC technique with data from the Moderate-resolution Imaging Spectroradiometer (MODIS) and Sea-Viewing Wide Field-of-View Sensor (SeaWiFS) and *Chevallier et al*. [2014] applied MCC to SST data from the geostationary Spinning Enhanced Visible and InfraRed Imager (SEVIRI) sensor. *Choi et al*. [2013] and *Yang et al*. [2014] estimated ocean currents using an approach similar to MCC applied to the Korean Geostationary Ocean Color Imager (GOCI) estimates of total suspended matter and compared their velocity estimates with in situ measurements from a buoy. *Hu et al*. [2016] also use MCC applied to GOCI estimates of total suspended matter data to derive tidal currents.

The MCC technique has the advantage of requiring minimal user input compared with many other feature-tracking techniques [*Matthews and Emery*, 2009] making it a very attractive method for automation. The major limitation for velocity estimation is the quality of the data. Performance is sensitive to cloud cover and feature distortion, and therefore temporal resolution of data. Even with such limitations, previous studies have estimated velocities with root mean square (RMS) errors of 10 – 25 cm s^{-1} compared against in situ and remote-sensing measurements [*Tokmakian et al*., 1990; *Bowen et al*., 2002; *Crocker et al*., 2007]. However, with the exception of *Bowen et al*. [2002] and *Matthews and Emery* [2009], there have been no studies to the authors' knowledge that have applied the MCC technique to retrieve ocean currents routinely. For a routinely operated method it is important to fully characterize the approach, including analysis of its limitations such as cloud cover.

The European Space Agency's *GlobCurrent* project is concerned with developing a global ocean surface current product through synergistically combining model, in situ and remote sensing data (www.globcurrent. org). Toward this aim the project is investigating and evaluating the use of MCC with modern satellite data. GOCI is a visible spectrum (ocean color) sensor in geostationary orbit above the Korean Peninsula which captures 8 (500 m spatial resolution) scenes a day at hourly intervals. This means that GOCI data provide a

radically new opportunity to evaluate the MCC technique given the high temporal resolution of the data, whereas most previous applications and assessments of MCC have been limited by slow repeat times between successive satellite observations. With proposed future geostationary missions, such as Ocean Color Advanced Permanent Imager (OCAPI) [*IOCCG*, 2012], providing hourly images at ground sampling resolution of 250 m, the use of MCC for surface ocean current measurements may become increasingly useful.

In this paper we present a MCC approach applied to the hourly GOCI data to estimate surface ocean currents, the results of which are verified against HF radar data to determine the accuracy and operating limits of the technique. The paper is organized as follows. Section 2 discusses the GOCI data, the HF radar data, and the simulations used to optimize the MCC parameters. Section 3 describes the methods and how parameters have been derived from the simulated data sets. Section 4 describes an assessment of the GOCI data including analysis of the impact of missing data and degradation in geolocation. Section 5 discusses the accuracy of derived velocities from the GOCI data, as assessed using the HF radar data, before showing potential further analyses in section 6 and finally summarizing, discussing and concluding in section 7.

2. Data

The primary data sources used within this study are GOCI data, HF Radar and synthetic data sets. Each data set is briefly introduced in this section following the description of the test site.

2.1. Geographical Region

The Tsushima (Korea) Straits (called Tsushima Straits for the remainder of this manuscript) is an area of water between South Korea and Japan. The dominant current feature present in this region is the Tsushima Warm Current, with mean velocity (for the period 1995–2009) of between 12 cm s^{-1} and 25 cm s^{-1} [*Ito et al.*, 2014] flowing in a northeasterly direction. Seasonal variations in the surface current have been described by *Yoshikawa et al.* [2010]. *Takikawa et al.* [2003] have shown that there are also strong tidal currents in the region, dominated by M2 (principal lunar semidiurnal) tidal constituent, with peak speeds up to 40 cm s^{-1}. The bounding box used for the accuracy assessment of MCC derived velocities covers the area: 32.64 – 36.09°N, 126.88 – 131.61°E.

2.2. GOCI Data

The GOCI instrument, aboard the Korean Communication, Ocean and Meteorological Satellite, acquires data in 8 bands in the visible and near infra-red spectrum, spanning the range 400–865 nm. It provides complete coverage 8 times a day of a 2500 km × 2500 km section of the Earth's surface centered on the Korean Peninsula (Figure 2a). To achieve its intended ground resolution of 500 m, the 2 mega-pixel detector views 16 "slots" of the whole scene in sequence, building up the image for each wavelength filter in turn before moving on to the neighboring slot. The full view is then constructed from this 4 × 4 array of overlapping slots. A detailed description of this is given in *Faure et al.* [2008], who also note that neighboring slots may be
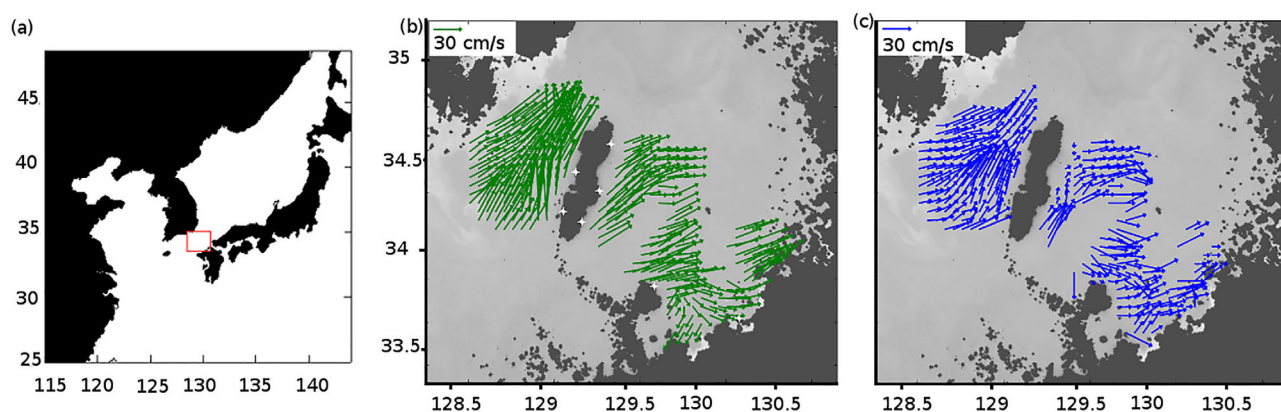

Figure 2. (a) Total region covered by the GOCI sensor with the red box indicating the Tsushima Strait area used in this study; (b) arrows indicate mean velocities from HF radar and locations of the 7 HF radar stations are shown as white dots; c) arrows indicate mean velocities from MCC methodology. Data are from 26 March 2012 and all MCC image pairs have been used. Velocities are the mean over corresponding time periods and locations. Radar-derived velocities are only shown where there are MCC velocities.

observed up to 15 min apart, so some apparent spatial discontinuities can occur due to feature movement within this time lag. *Oh et al.* [2012] modeled the pathways of stray light within the instrument and showed that reflections from the structure and mirrors could generate variable lightening toward the edge of images, and that that would vary with solar zenith angle and hence time of day.

Data that contained both individual normalized water-leaving radiances (nLw) at each of the 8 channels and the estimated chlorophyll concentration have been used in this study. The accuracy of these products has previously been verified by *Wang et al.* [2013]. However, here the consistency of values is more important than the absolute accuracy, as the MCC technique relies on relative values between two images. The hourly observations are at 0:30–7:30 UTC (corresponding to ∼09:30 to 16:30 local solar time in our focal region), so the effects of sunglint may be more prominent in the middle of any daily sequence.

2.3. High Frequency Radar

High frequency (HF) radar systems can be used to measure the speed and direction of surface currents, in any weather 24 h a day and networks of ground stations can be used to monitor large areas of coastal and near coastal waters [*Chapman et al.*, 1997]. Here, MCC-derived current estimates are compared against HF radar data provided by a network of stations in the Tsushima Strait (Figure 2b). The method for matching HF radar and MCC velocities is described in section 5.1.

Reliable vector currents can only be derived for regions viewed by 2 or more individual radar stations. The HF radar data used here were supplied on a 0.025° resolution grid. Further information about the HF radar network used in this study is detailed in *Yoshikawa et al.* [2006]. The radar scans are averaged and combined to give hourly velocity fields. Comparisons with multiple vessel-mounted ADCP instruments showed that the error in the individual HF radar-derived currents is ∼10 cm s^{-1} [*Yoshikawa et al.*, 2006].

2.4. Synthetic Data

Simple synthetic data sets were created to verify the MCC implementation and for use in the sensitivity analyses. The data sets consist of a solid disc with a horizontal translation applied between template and master images and a layer of Gaussian random noise applied (see Figure 1). The same translation is applied in all cases. The added noise had zero mean but in each case a different standard deviation, ranging from 0 up to 0.24 times the contrast between the disc and background. This allowed the MCC sensitivity to the signal-to-noise ratio (SNR) and to the size of the pattern template to be evaluated.

A particular challenge is the presence of variable gaps in the spatial data within both the template and master images, whether due to land or to clouds (see Figure 1). Therefore we created a second synthetic data set of solid discs (with known translation) plus additive Gaussian noise with the addition of missing data. The amount of missing data ranged from 0 to 80% of the image pixels in increments of 5%. Two procedures for generating missing data were followed: a random uncorrelated distribution (salt-and-pepper) and a spatially correlated distribution (ellipsoids). In the latter scenario, cloud is generated as a series of elliptical patches of certain size. This is a very simple approximation to the spatial correlation of real cloud cover.

3. MCC Method and Its Evaluation With Synthetic Data

The basic foundation of the MCC technique is illustrated in Figure 1, where for each template in the first image (i.e., the area highlighted by the box in Figure 1) a search is made for a corresponding pattern in the second image, with the measure of agreement being the cross-correlation of the two. Of all possible matches in the second image, the match with the highest cross-correlation is deemed to represent the motion within the scene. Difficulties can arise due to inconsistencies between the two images (e.g., geolocation errors, data calibration), measurement errors, image noise (e.g., sensor noise) and gaps with no value (representing land or clouds) and these are likely to be present in optical remote sensing data. Assuming consistent measurement, calibration and geolocation between images, the remaining issue to overcome is that of cloud. One approach to overcome this in the data is to interpolate and fill in the cloud values, but this is not straightforward as ideally the resultant image should retain the sharp gradients present in the unobscured data. Instead, we adopt the masked normalized cross-correlation technique as developed by *Padfield* [2012] for the registration of medical imaging. This method allows an efficient way to calculate MCC, using Fourier transforms, without masked regions (in this case regions of land and cloud) entering

into the correlation calculation. This method adapts the classic equations with the addition of two mask arrays resulting in the formula:

$$NCC = \frac{f^{-1}\left(F_1.F_2^*\right) - \frac{f^{-1}\left(F_1.M_2^*\right).f^{-1}\left(M_1.F_2^*\right)}{f^{-1}\left(M_1.M_2^*\right)}}{\sqrt{f^{-1}\left(f(I_1.I_1).M_2^*\right) - \frac{\left(f^{-1}\left(F_1.M_2^*\right)\right)^2}{\left(f^{-1}\left(M_1.M_2^*\right)\right)}}\sqrt{f^{-1}\left(M_1.f(I_2'.I_2')\right) - \frac{\left(f^{-1}\left(M_1.F_2^*\right)\right)^2}{\left(f^{-1}\left(M_1.M_2^*\right)\right)}}}$$

where NCC is the normalized cross correlation, f and f^{-1} are the Fourier and inverse Fourier transforms, I_1 and I_2 are the two images, F_1 and F_2 the Fourier transforms of I_1 and I_2, M_1 and M_2 are the Fourier transforms of the masks associated with I_1 and I_2', ' denotes rotation by 180 ° and * denotes a Fourier transformed rotated array. The interested reader is directed to *Padfield* [2012] for the derivation of this equation.

Algorithm parameters that will affect the MCC-derived velocities include: template window size, the number of masked pixels and the master search window size. These are discussed in the following sections.

3.1. Master Search Window Size

For each template window a larger corresponding search window was selected from the master image based on the template position and the expected maximum velocities within the region. Given the generally observed currents (see section 2.4) this study used 1 ms^{-1} as the maximum expected velocity.

3.2. Sensitivity to Template Size

The performance of the technique depends upon the signal-to-noise ratio (SNR) i.e., the ratio of the true signal to the RMS of the noise. Clearly the technique should work perfectly with negligible noise and is likely to fail when the noise swamps the signal.

A key operating choice is the size of the template window being matched between scenes. With the one-feature simulations good agreements can only be expected for a template containing to some extent both disc and background. A very large template window will be impractical because it will be unable to resolve spatial variations in surface current that are smaller than the window width. Figure 3 shows the result of a series of simulations varying both template size and SNR (by increasing the Gaussian noise standard deviation). Each simulation has been repeated 20 times and the mean taken. If the template is significantly smaller than the disc then the shape of the feature bounded by the template (the angle and curvature of the border) is not unique to a particular location 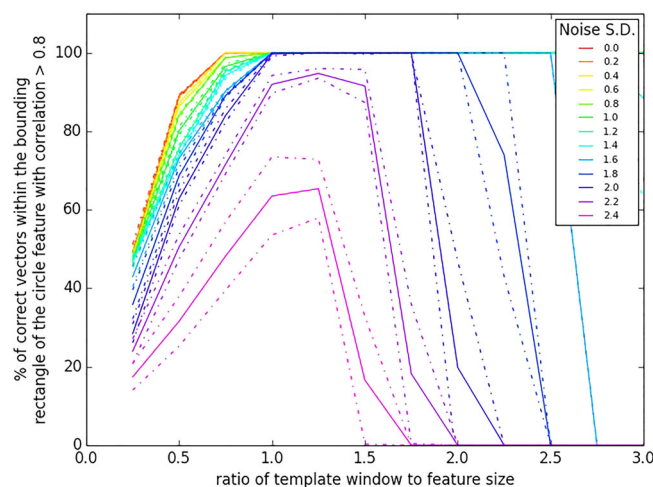around the disc. As the template becomes commensurate with the disc diameter the performance of the algorithm improves, but declines for much larger template windows especially when coupled with high noise levels. The effect of increasing noise is to reduce performance, as expected. Only vectors with correlation above 0.80 have been included here following the 95 percentile threshold used by *Tokmakian et al.* [1990] for raw SST images. The results of Figure 3 are used as a guide that the template should be of a similar size to the dominant features to be followed, which agrees with the recommendation of *Kamachi* [1989].

Figure 3. Performance of MCC procedure with simulated data as a function of template window to feature size ratio and level of added noise (different colored lines). The contrast between values in the disc and background is 10, therefore added Gaussian noise of mean 0 and standard deviation (SD) = 2.4 represents the lowest signal to noise ratio used. For each scenario, 20 realizations were performed: the solid lines represent the mean performance (proportion of correct vectors derived from MCC with correlation greater than 0.8, the correlation threshold used in *Tokmakian et al.* [1990]) and the dotted lines are ± 1 standard deviation.

3.3. Sensitivity to Missing Data

The effect of missing data (primarily due to clouds, poor light conditions or sunglint) is evaluated in order to determine what level of missing data makes the algorithm unreliable, using both salt-and-pepper style missing
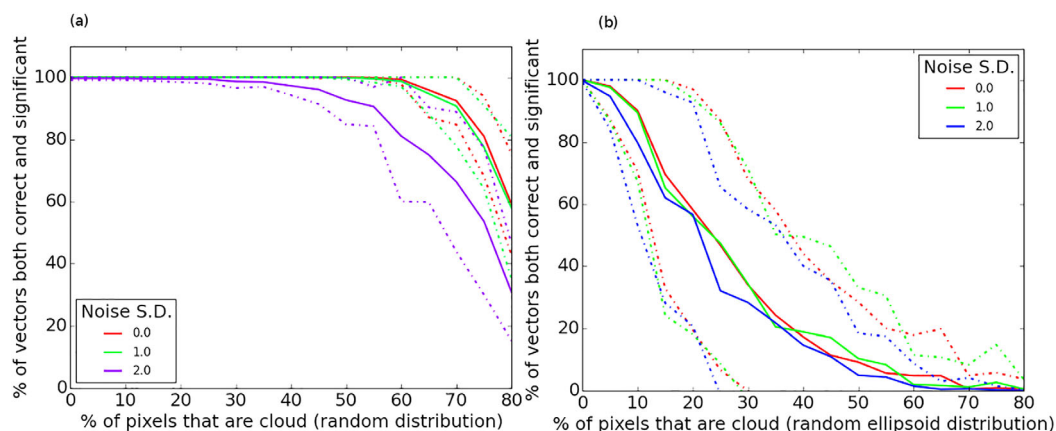
Figure 4. The effect of synthetic cloud (i.e., missing or occluded data) on the MCC results at 3 levels of additive Gaussian noise. The template size to feature size ratio is fixed at one, and the solid and dotted lines represent mean and ± 1 standard deviation (from multiple realizations). (a) Totally uncorrelated (salt and pepper) cloud; (b) Spatially correlated clouds (ellipsoids).

data and spatially correlated missing data. This is to simulate the effect of cloud and poor light conditions. Each salt-and-pepper occluded data simulation has been repeated 20 times with the mean taken with varying noise. The spatially correlated occluded data simulations have been repeated 100 times, since they show much higher variation, with the mean taken.

Figure 4a shows that increased salt-and-pepper missing data does not reduce the ability of the algorithm noticeably, for low noise levels, until approximately 60% missing data. However, as missing data levels increase, the number of pixels that the cross-correlation uses reduces and therefore lowers the significance of the correlation. Figure 4b shows that when the missing data are spatially distributed (i.e., a more realistic case) the effect is much more profound. With 15% of data missing, the performance (as rated by percentage of correct vectors identified) has dropped on average to 80% of the maximum achievable. Increasing missing data to 30% reduces the algorithm performance to 30% of maximum. It should also be noted that the significance of the correlation may also be reducing as missing data increases. A missing data level of 15% (in both template and master images) equates, on average, to approximately 25–30% of missing data in the combined overlap region that the correlation is computed on. These results are used to set a maximum threshold level of 25% missing data in the combined overlap for which the MCC algorithm is expected to have a success rate of 80%.

4. Initial Assessment of GOCI Data Quality

Before implementing and evaluating the MCC technique applied to GOCI data (section 5), an initial assessment of the consistency and usefulness of GOCI data for monitoring features was undertaken. Three analyses have been performed: image registration, cloud coverage, and inspection of image discontinuities.

4.1. Image Registration

Accurate and precise registration of the data, both between different images and with respect to the Earth's surface, is important as any offset or registration error will propagate into the derived velocity estimates. To verify the consistency between images, a sequence of 30 consecutive GOCI images with the same visible land feature (a small island) were examined qualitatively by eye. In the worst case the feature may have moved by a pixel (500 m for GOCI) but this could also be due to optical effects of shadowing and sun angle.

Faure et al. [2008] explain that the double-mirror system used to separately focus on the 16 slots should provide position accuracy of the order of a pixel. *Yang and Song* [2012] state that the geometrical quality requirements for GOCI are ~1 km at nadir which equates to 2 image pixels. In their study they found frame-to-frame registration accuracies better than 1 pixel. To compare GOCI-derived products against in situ data it will be important that the absolute geolocation is accurate. A qualitative analysis using coastline vector data and geocorrected GOCI imagery suggests that that the absolute geolocation is correct to within the 1 km requirement for GOCI.
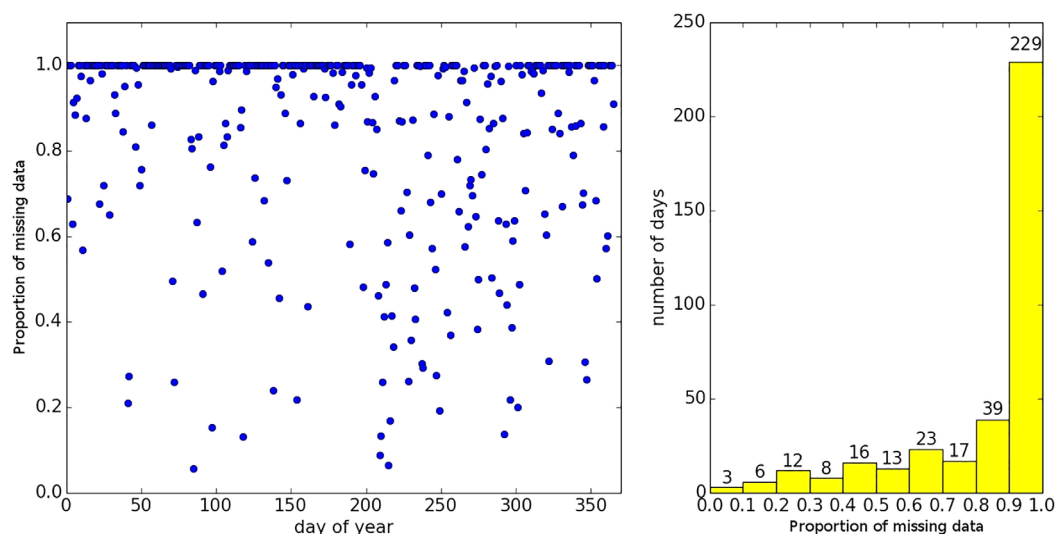
Figure 5. Daily median missing data in the Tsushima Strait region: (a) value for each day in 2012, (b) histogram analysis of missing GOCI data. There were 9 days in 2012 with less than 20% missing data.

4.2. Cloud

As cloud is a limiting factor for deriving velocities using the MCC technique (see section 3.3), the cloud statistics within the GOCI data record were assessed. As cloud pixels are masked out in the GOCI products, this analysis is on the masked pixels which do not correspond to land, so could also include pixels masked due to poor light conditions. Data for 2012 were analyzed limited to the Tsushima Strait region containing our HF radar data. For each scene from each day the fraction of masked pixels was determined, excluding land, with the median value calculated for each day (Figure 5a). It can be noted that the region has a high proportion of masked pixels throughout the year. A histogram analysis (Figure 5b) shows that the majority of scenes have > 90% masked pixels in this region, with fewer than 50 days having less than 50% masked pixels and only 9 days with less than 20%. Cloud cover (on the full GOCI scene) is also a limiting factor on the geolocation accuracy of the data [*Yang and Song*, 2012] as it may obscure landmarks used for registration. Independent ground-based observations (Japan Meteorological Agency data for station Fukuoka, in the south of Tsushima straits, http://www.data.jma.go.jp/obd/stats/data/en/smp/index.html) suggest that the annual mean cloud amount in this region for 2012 was approximately 72%, the joint highest value since 1931.

4.3. Image Discontinuities

Visual inspection of the GOCI images identified artefacts due to the acquisition and processing techniques employed which show themselves as lines of discontinuity as seen in Figure 6. These are located at (or near) the boundaries of the 16 slots, but have been observed to move relative to ground features after geo-correction (presumably corresponding to changes in pointing of the satellite sensor). When considering data across the whole of the 2012 archive there is a large local variation in the positioning of these discontinuities, with an observed movement of 22 image pixels measured on images acquired on 3 August 2012. This could have an effect on MCC detection methods as the discontinuity will appear as a feature on the two images causing erroneous velocities to be detected. Furthermore, the discontinuities are not a simple straight edge but "zig-zag" at the corner joints (see Figure 6). Since they appear to move between images a simple masking approach is not possible. The Tsushima Straits region, being at the center of GOCI coverage, lies within the join of 4 slots and suffers from these discontinuities. These features at the border between different slots may be seen in the individual radiances, especially 412 and 490 nm [see *Wang et al.*, 2013], and thus they also appear in the standard chlorophyll product; *Hu et al.* [2012] suggest that an alternative linear chlorophyll algorithm may reduce the prominence of these discontinuities.

4.4. Errors Due to Recurring Physical Features

To reduce the chance of unrelated features being accepted as matching, a minimum value for the cross-correlation is necessary to reduce the chance of a moderate correlation between one feature and a
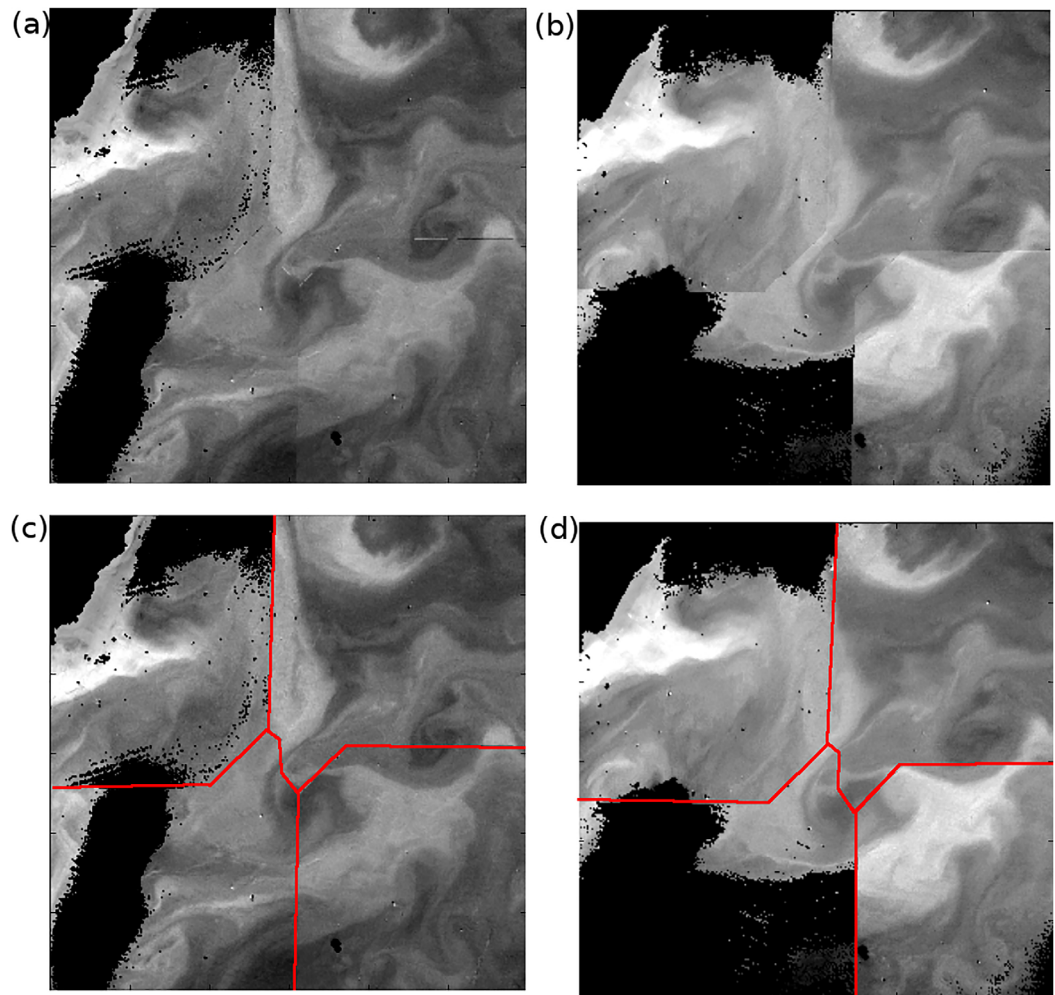
Figure 6. GOCI image discontinuities. Image shows the chlorophyll product from 3 August 2012 (a and c) hour 1 and (b and d) hour 6, where the (c and d) bottom images are the same as the (a and b) top ones with the discontinuity joins of four slots annotated. Each image covers the same geographic coordinates and the features are present in all channels.

completely different feature in a later image being selected. The approach of *Tokmakian et al.* [1990] has been followed with the MCC algorithm applied to two scenes 6 months apart to determine an upper bound on the cross-correlation that may be achieved between images with completely independent features within them. This can be used as a threshold to filter the correlations allowing us to quality control the results by removing those correlations with a value less than this threshold. *Tokmakian et al.* [1990], using raw SST images a year apart, identified a correlation value of 0.8 which corresponded to the 95th percentile of all the maximum correlations. Table 1 shows the corresponding 95th percentiles of the correlations for MCC applied to each of the GOCI products.

Table 1. MCC Correlation[a] 95th Percentiles

Band/Product	1	2	3	4	5	6	7	8	Chl
Wavelength (nm)	412	443	490	555	660	680	745	865	
Color	Blue	Blue	Blue	Green	Red	Red	Infra-red	Infra-red	
Correlation	0.83	0.78	0.81	0.72	0.62	0.85	0.63	0.63	0.77

[a]Calculated from images on 16 February and 16 August 2012.

5. Evaluation of MCC Technique Applied to GOCI Data

This section describes the application of the MCC method to GOCI data, the quality control regimes and the coregistering and verification of MCC derived velocity vectors with HF radar derived vectors. For each pair of scenes, known as master and slave (see Figure 1), the slave image is windowed into smaller template scenes.

The water channels either side of Tsushima Island are ~40 km at their narrowest, with individual circulation features being roughly half that size. The simulation results show the template size should match the physical feature size (see Figure 3), therefore a template of 44 × 44 pixels i.e., 22 km square was employed. This is the same size as used by *Emery et al.* [1986], *Matthews and Emery* [2009], and *Crocker et al.* [2007]. The MCC was then performed with each of these templates estimating a velocity, the result being a vector field of velocities for each master-slave pair. Each template window was shifted by approximately 25% such that neighboring windows overlapped by 75%. The template window shift is a pay-off between a denser vector field and processing time. Overlapping windows means that neighboring vectors are not independent measurements.

Quality-control filtering was performed on the velocity vectors. As previously mentioned, correlations calculated from less than 75% pixels (i.e., more than 25% missing data) were rejected. Each vector has an associated correlation value from the template matching; rudimentary filtering was achieved by discarding vectors with correlation less than the thresholds derived in section 4.4. Further filtering was performed using neighborhood vector magnitude and angle information similar to that described in *Crocker et al.* [2007]. Such filtering is important to remove erroneous estimates, but does imply that the effective spatial resolution of the technique is not as fine as the grid on which it was calculated. A square window of 5 × 5 pixels was applied to the vector field, centered on each vector in turn, with the center vector discarded if there were less than 3 other vectors within the window. The center vector magnitude in u and v must also agree with at least 3 neighboring vectors to within 0.1 ms^{-1} [*Crocker et al.*, 2007]. Also, maximum correlations that were identified on the edge of the search boxes were ignored, as it was unclear if the peak maximum was actually outside of the search box.

Figure 2c shows a mean averaged velocity vector field determined using the MCC approach on all acquisitions from 26 March 2012. The corresponding HF radar vector field (only showing radar scans at the same point as the MCC and averaged over the same time period) is shown in Figure 2b.

5.1. Coregistration With HF Radar Vector Field
The implementation of the MCC technique enabled current estimates at a spatial resolution of ~5 km, whilst the HF radar data are supplied on an approximate 2.5 km grid. To compare the two data sets at each MCC vector location a mean is calculated of all the HF radar observations that fall within the area defined by the MCC template window (22 km × 22 km) at that location. Thus both data values are an integration of surface velocities over the same spatial area. A mean is then taken of the HF radar observations over the same time period as defined by the GOCI image acquisitions.

5.2. Data Selection
Some implementation decisions have to be made in order to evaluate the MCC technique with GOCI data in our chosen area. A critical decision is the time separation of images to be used. Short periods imply that the feature is likely to have been translated without significant evolution of its shape; however, for images an hour apart, the resolution of the data (here 500 m) precludes the algorithm from resolving currents less than 500 m hr^{-1} i.e., ~14 cm s^{-1}. Longer time separations enable improved velocity resolution. However it is then only returning a mean over that interval and ignoring shorter-term variations, meaning that changes in shape, orientation and intensity contrast of features may become important.

Missing data affect both the algorithm performance and significance of correlation. To evaluate this impact, 4 days from 2012 were selected which had low (<15%) median missing data over the test site: 26 March, 28 April, 29 July and 3 August. The MCC analysis and filtering was then performed on each image pair from each day for each product. Each day there are 8 GOCI acquisitions, therefore for each product there are 28 possible pairs of images to estimate velocities in a day (seven pairs with 1 h separation, six with 2 h separation etc.). This gives the possibility of observing surface currents derived from one hour up to 7 h intervals. The results from these 4 days have been combined in the following analyses.
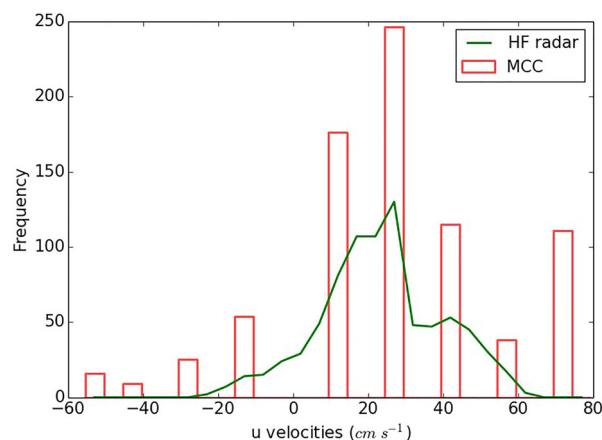
Figure 7. Heavy quantization visible in the MCC derived vectors (red bars) compared to the HF radar velocities (green line) due to the time interval between master and slave images of 1 h. Both MCC and HF radar velocities are binned in 5 cm s^{-1} bins. These data shown are for nLw_412, all other products show similar quantization (not shown here).

5.2.1. Velocity Distribution

For each of the 7 time intervals, the distribution of velocities derived from the MCC technique has been compared to that of the HF radar. The results can be seen in figures 7 and 8. Figure 7 shows the velocities derived from 1 h separated data from nLw_412. It can be seen that the MCC-derived velocities (red) suffer from heavy quantization due to the velocity resolution discussed in section 5.2 (14 cm s^{-1} for 1 pixel movement – therefore no smaller positive velocity can be identified). This means that a resulting velocity field will have low precision. One and 2 h separated data are therefore disregarded for the remainder of this manuscript due to this limitation. Time periods of 3, 4, 5, 6 and 7 h are examined together as these results show similarities.

Figure 8 shows the velocity distribution, in u (zonal - longitudinal) and v (meridional - latitudinal), for nLw_412, nLw_660 and chlorophyll products. These three products have been selected to show the results from a blue channel, red channel and a derived product. Qualitatively they look similar but there are some differences in mean velocity, in particular for the nLw_660 product, which shows a ∼20 cm s^{-1} difference (between MCC and HF radar derived velocities) in the mean u velocity and ∼13 cm s^{-1} in the mean v velocity.

The number of MCC vectors identified above the correlation threshold gives an indication of each product's performance. nLw_443, nLw_490 and nLw_555 and chlorophyll resulted in 2 - 3 times more vectors being identified than from nLw_660, nLw_680, nLw_745 and nLw_865 (see Table 2). This is likely to be due to stronger in-water absorption in these latter bands (resulting in weaker reflected signal and less identifiable features). The near-infra-red bands (nLw_745 and nLw_865) will mostly contain sunglint information for atmospheric correction purposes rather than water content information, and therefore weaker water leaving radiance features to match against.

5.2.2. Velocity Magnitude Comparison

Table 2 shows the RMS difference and Spearman correlation coefficient between the MCC and HF radar in u and v for each product calculated for time periods of 3, 4, 5, 6 and 7 h separation together with the number of observations. The Spearman correlation coefficient has been used in preference to the Pearson correlation coefficient because the MCC velocities are an interval data set (not continuous). Products nLw_660, nLw_680, nLw_745 and nLw_865 have fewer observations and higher RMS errors than the other products, with nLw_490 showing the lowest RMS and highest correlation, suggesting this product provides the optimal agreement between the MCC and HF radar derived velocity fields. Identical results are noted for nLw_745 and nLw_865. It was found that, for those pixels which had passed the cloud masking, the radiance values in nLw_865 had magnitude of approximately 38% of those in nLw_745. A near-constant scaling for each pixel results in identical cross correlation results. These 2 near-infra-red bands will show sunglint under clear skies and very little surface content. For the rest of this manuscript, only nLw 412 - 555 and chlorophyll products are considered, as Table 2 shows that nLw 660 - 865 have reduced performance compared to that of the nLw 412 – 555 products.

Looking at density scatter plots of Figures 9a and 9b, it can be seen that there is quite a large spread but with the majority of points close to the 1:1 line. The regression fit (solid) lines in Figures 9a and 9b have gradients close to 1 (1.41 and 1.02 for u and v respectively). The RMS velocity values of the data are 19.4 cm s^{-1} and 22.6 cm s^{-1} for u and v respectively.

5.3. Analysis for Routine Operation

To evaluate the MCC algorithm's capability for routine application it was decided to analyze more days. Only days with a median missing data of 50% or less over the test site were considered (a total of 46 days).
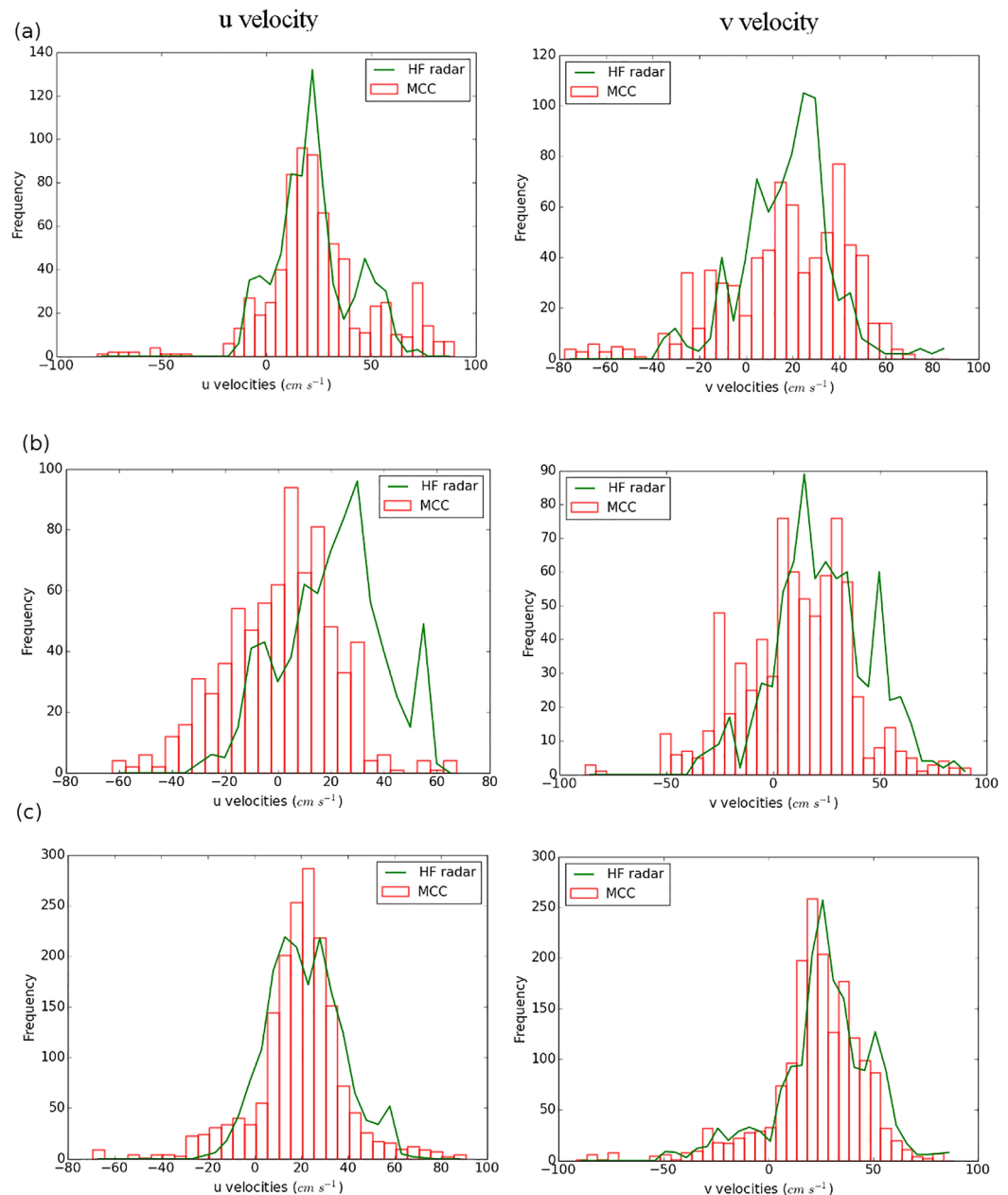
Figure 8. Distributions of MCC (red bars) and corresponding HF radar-derived (green line) current velocities in (left) u and (right) v directions. Data are for (a) nLw_412, (b) nLw_660, and (c) chlorophyll, all with time periods of 3, 4, 5, 6, and 7 h. All data are binned in 5cm s^{-1} bins.

Table 2. Statistics for Velocity Differences of Each GOCI Product[a]

Product	nLw	nLw	nLw	nLw	nLw	nLw	nLw	nLw	Chl
Wavelength (nm)	412	443	490	555	660	680	745	865	
Color	Blue	Blue	Blue	Green	Red	Red	Infra-red	Infra-red	
N[b]	736	1783	1537	2368	743	610	704	704	1743
RMS u	22.4	21.1	17.1	18.5	30.9	33.6	31.3	31.3	19.3
RMS v	28.1	21.7	17.9	22.5	35.9	42.9	37.0	37.0	24.7
r_ρ[c] u	0.52	0.61	0.72	0.61	0.29	0.27	0.27	0.27	0.44
r_ρ[c] v	0.42	0.66	0.72	0.61	0.09	−0.11	0.09	0.09	0.49

[a]Differences between HF radar and MCC velocities for the 8 nLw and chlorophyll products from the 4 dates in section 5.2.
[b]The number of observations used in the RMS calculation.
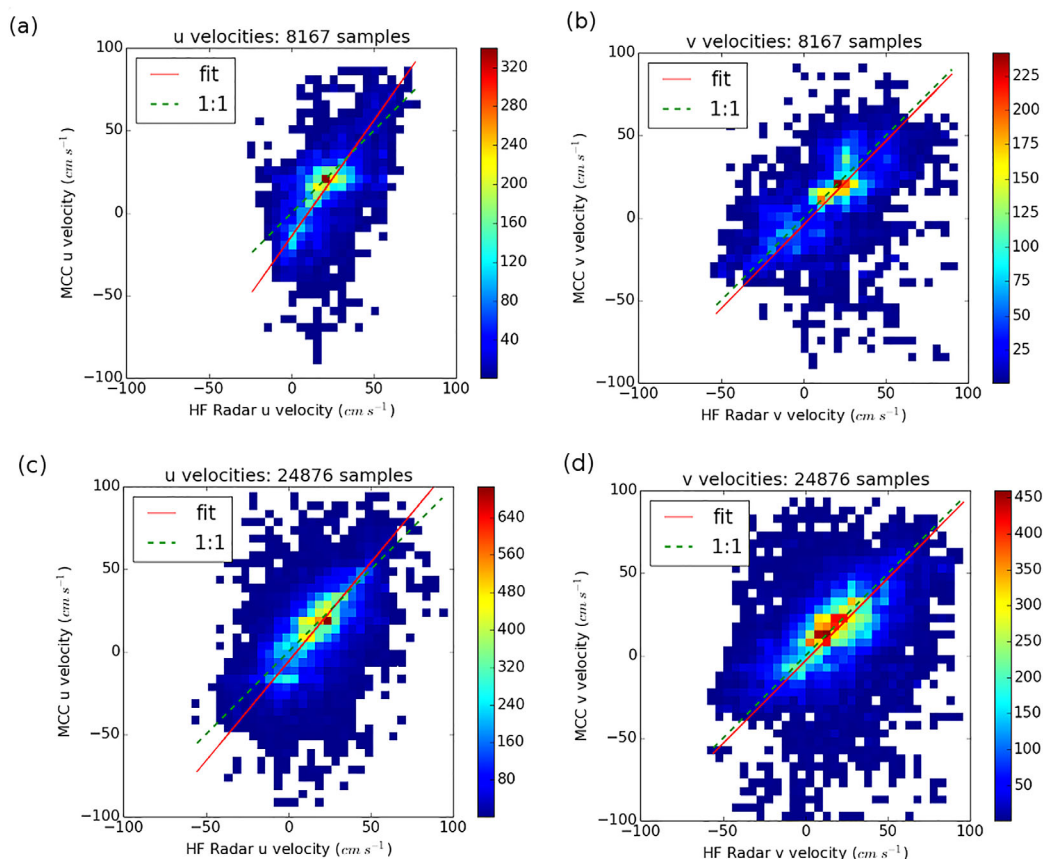[c]Spearman correlation coefficient between HF and MCC velocities.

Figure 9. Density plots of MCC versus HF radar (left) u and (right) v velocity components for nLw products 412–555 and chlorophyll for (a and b) time separations 3, 4, 5, 6 and 7 h with 4 days combined, and (c and d) 46 days with < 50% cloud coverage. The data have been binned in 5 × 5 cm s^{-1} bins, with the color denoting the number of vectors per cell. Both plots show the 1 to 1 line (dashed) and the orthogonal regression fit line (solid). The RMS values for these data are (a) 19.4 cm s^{-1}, (b) 22.6 cm s^{-1}, (c) 18.3 cm s^{-1}, and (d) 23.0 cm s^{-1}.

Chlorophyll and nLw products 412 - 555 were considered. The combined results are shown in the density scatter plots of Figures 9c and 9d. These show similar results to the initial highly selective data in Figures 9a and 9b and the u and v components have RMS values of 18.3 cm s^{-1} and 23.0 cm s^{-1} respectively. This shows that with the use of appropriate quality control (e.g., a threshold for minimum acceptable correlation and near-neighbor consistency checks) a comparable accuracy can be achieved using images with 50% cloud cover as to the best images, albeit with fewer vectors returned. As expected (results not shown here) the fewer missing data regions the more dense and wider the vector field identified. Hence, to routinely derive a dense vector field, images free of missing data are required or else a procedure to interpolate the current velocity estimates across the occluded regions should be included.

5.4. Effect of Discontinuities

To give an indication of the effect of the discontinuities, 8 images for 3 August 2012 were examined to note the location of the discontinuities in each acquisition. All derived velocities beginning or ending in these regions, or whose template window would have coverage in these regions, were then masked out, leaving 517 vectors across the chosen products and range of time separations. The result of such editing was a minor increase in RMS errors for that day, indicating that these features are not a major contribution to the overall errors in this test case. The automatic masking of discontinuities is nontrivial (as explained in section 4.3) making this a difficult problem to analyze fully over multiple days.

6. Potential Oceanographic Applications

In the previous sections it has been demonstrated that the MCC technique can be applied efficiently and robustly to GOCI data, with the errors in each component being of the order of 20 cm s^{-1}. Clearly such a
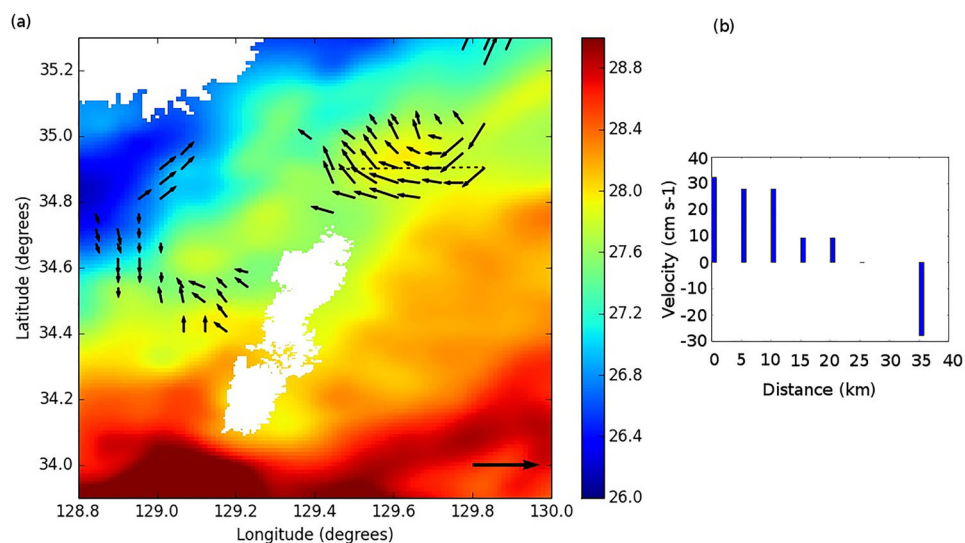
Figure 10. Identification of an eddy feature to the northeast of Tsushima Island. (a) Background shows sea surface temperature (° C) from the Multi-scale Ultra-high Resolution Sea Surface Temperature product available from http://mur.jpl.nasa.gov/. Current vectors are calculated from two GOCI scenes with a separation of 3 h acquired 30 July 2012. Reference current (bottom right) is 1 ms^{-1}. (b) Meridional velocities along 35 km length transect described by dotted line in Figure 10a going from West to East.

technique is more usefully applied in a region of significant currents rather than weak drift. The area around Tsushima Island is well-monitored by the HF radar system, providing day and night measurements. Although GOCI cannot match that high temporal and spatial resolution, in regions beyond the range of HF radar systems, the MCC technique can usefully add to our knowledge of strong, surface ocean velocities, currents and tides.

6.1. Eddy Currents

Figure 10 shows an eddy 33 km to the northeast of Tsushima Island, whose anticyclonic flow is consistent with the slightly warmer core indicated by sea surface temperature. In addition to tracking such features, the MCC technique can also be used to quantify the magnitude of the surface velocities around the eddy. Figure 10b shows meridional velocities for a section across the eddy, with a change from $+30$ cm s^{-1} to -30 cm s^{-1} over 35 km. This is commensurate with the branch of the Tsushima Warm Current in the eastern channel having an average speed of 26 cm s^{-1} [*Takikawa et al.*, 2005] and Figure 3 of that paper showing a pair of eddies with changes of ± 20 cm s^{-1} over 25 km. Eddies in this region are associated with the Tsushima Warm Current flowing up the channel to the east of the islands. The study by *Takikawa et al.* [2011] relied on several days ship time to map the eddy flow field in this region. An improved understanding of the currents to the east of the Korean peninsula is essential for monitoring the transport of harmful algae [*Kim et al.*, 2016], so all techniques that give high-resolution quantitative information on the flow field will assist in the prediction of such blooms.

6.2. Tidal Currents

Figure 11 shows a region in the southwest corner of the Yellow Sea (800 km west of Tsushima Island), where several consecutive days of reduced cloud cover permit the M2 lunar tidal period to be assessed. The data coverage is too sparse for a satellite-only estimation of the dominating tidal component of the surface velocity, but estimates using GOCI data could be assimilated into numerical models for studies of this area. These tidal currents of up to 150 cm s^{-1} are a major concern for this region because of their effect on the transport of sediments from the Chianjiang River [*Bian et al.*, 2013]. Knowledge of sediment transport in this region is important for environmental conservation, sustainable development and reduction of pollution [*Yang et al.*, 2003]. Figure 11 demonstrates that the directional change in surface velocities related to the tide is the dominant hydrographic process. Surface velocities range between ± 100 cm s^{-1} which appear consistent with the ranges identified by previous in situ studies [*Bian et al.*, 2013]. Improved knowledge of tidal currents is also clearly important for efforts to minimize fuel usage (and therefore emissions) by freight ships. This cannot be achieved with satellite data alone, but such data from GOCI could be used to help
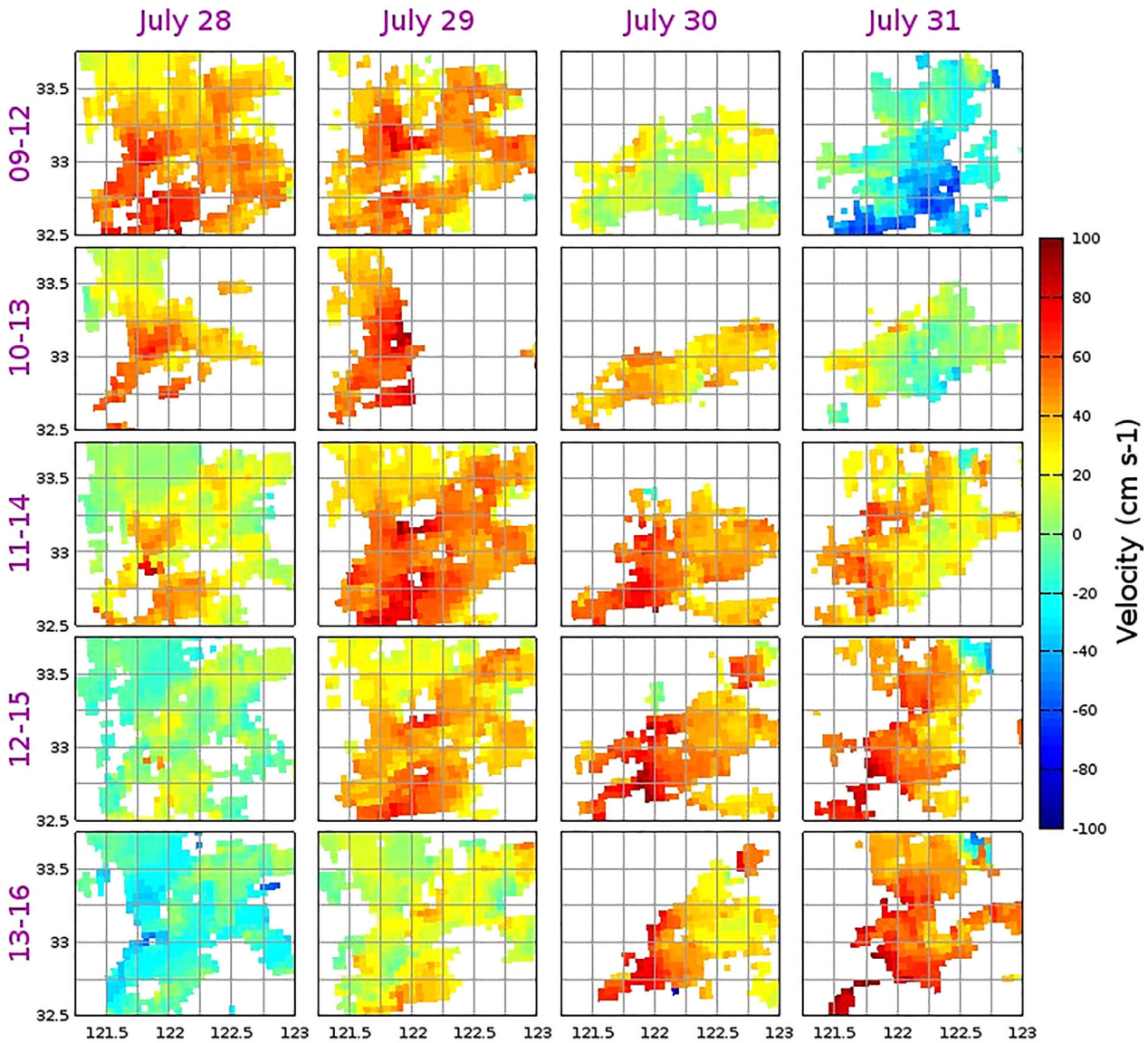
Figure 11. Surface current velocities derived from the MCC technique in the southwest Yellow Sea. Each pane shows the surface velocities (u component only) over a specific 3 h time period (shown by time periods on y axis) for 4 consecutive days 28–31 July inclusive. Colors show velocity in cm s^{-1}. It can be seen that as the days progress the maximum current occurs later in the day.

further refine tidal models in this area and thus assist in the modeling of sediment transport [*Bian et al.*, 2013; *Gao et al.*, 2016].

7. Discussion

The MCC method is capable of deriving estimates of surface motion of the water in an automated fashion. Previous studies have shown results using remote sensing data such as MODIS, SeaWIFS and AVHRR, but have been disadvantaged by long repeat times of the satellite observations used. In this study, chlorophyll and water leaving radiance data from the geostationary GOCI sensor with an observation repeat period of 1 h have been used. The shorter repeat time of the observations, resulting in 8 images per day for each data product, gives an advantage of higher temporal correlation between successive scenes.

The Tsushima Straits region used to validate this study is a narrow strip of water between two land masses along with a selection of small islands. This results in a large proportion of masked pixels since areas of land

need to be removed from the data. The use of the masked normalized Fourier domain cross correlation can counter this but at the price of reducing the number of pixels used in the correlation calculation, hence reducing the significance of the correlation. The region is a complex environment where the eastern and western channels are dominated by different current components [*Yoshikawa et al.*, 2010]. This could influence the choice of time period between images to use in the MCC approach, as one may prefer to use an interval related to the period of the dominant current component. The GOCI data also suffer from discontinuities between the 16 slots that make up the full image, with the validation region coinciding with where the join of 4 slots occur. Template windows that contain one of these discontinuities may be adversely affected, although an investigation of one particular day showed this not to be a major problem.

Another major disadvantage of the MCC technique is occlusion. From the whole of the year 2012, an analysis showed that there were only 9 days where the validation region contained less than 20% masked pixels (excluding land). Shorter time intervals between repeat observations could reduce this to an extent but it will always be an issue for an optical sensor operating in the visible spectrum.

Velocities derived using a 1 h time separation have been shown to be heavily quantized (Figure 7) due to a combination of pixel resolution, repeat times and ocean surface velocity. The 500 m spatial resolution together with the 1 h separation results in a minimum velocity resolution of approximately 14 cm s^{-1}. It has also been shown that compared to HF radar measurements the MCC-derived velocities have similar distribution (Figure 8). Following on, the RMS and Spearman correlation values in Table 2 show that shorter wavelength bands (blue – green channels) and the derived chlorophyll product perform better than the longer wavelength bands (red – near infra-red). This is likely due to the optical properties of the water in this region giving stronger features at these shorter wavelengths, lower signal strength and higher absorption in the water at the longer ones and sunglint in the near-infra-red bands.

The density plots of Figure 9 show that the error spread is large but with a dense grouping close to the 1:1 line. The orthogonal distance regression fits show broad agreement to the 1:1 line. It can be seen from the regression fits (Figures 9b and 9d) that the v component of the MCC velocity shows a negative bias compared to the HF radar.

The RMS values in Table 2 do not imply that the error is purely within the MCC vectors. It should be noted that the HF radar measurements are also subject to error, i.e., hourly data (prior to averaging) have an RMS of approximately 10 cm s^{-1}, hence why the authors use an orthogonal distance regression rather than a simple least squares regression fit. Also the two techniques are making estimates of currents from different sources. The HF radar is measuring an average current velocity of the top 1 m [*Yoshikawa et al.*, 2006] of the ocean and is more accurate at measuring the radial velocity. The MCC observations are derived from tracking surface motion drift (up to optical depth) rather than any fundamental motion quantity. It relies on a trackable feature being present and recognizable in each image.

We have demonstrated that for the GOCI sensor the MCC results using the chlorophyll product are commensurate with those using water-leaving radiance products (for blue and green bands 1 - 4). The red and near infra-red water-leaving radiance bands (5 - 8) appear less suitable. For regions with average current velocities of 20 - 30 cm s^{-1} (such as the Tsushima Straits) short time separations of 1 and 2 h are not long enough to integrate over at the spatial resolution of 500 m, that is, the velocity resolution is not fine enough and heavy quantization is apparent. Results shown in this paper are a collation of analyses with time separations between 3 and 7 h. The optimal time period will depend on the resolution of the data and current velocities in the region. However, the 8 daily image acquisitions of GOCI give more opportunity for cloud-free data than, say, a single daily overpass by an AVHRR sensor.

The masked MCC approach allows velocities to be derived without cloud or land affecting the final result, albeit with a lower significance if there are large numbers of masked data. A suitable threshold should be selected to remove correlations calculated from a small number of cells. In this paper the threshold was based on a performance decrease to 80% based on simulated data tests. It has also been shown that the template window size should ideally be commensurate with that of the feature being tracked.

Most approaches to using MCC for surface current estimation have been implemented in open ocean regions, whereas here the approach is performed in the narrow channel of the Tsushima Straits. Where other approaches with GOCI data, such as that by *Hu et al.* [2016], have concentrated on using a few

high-quality nonoccluded images from a number of years, this study has exploited many images from the same year. The approach has been implemented in two scenarios over the Tsushima Straits: 4 days with $<$ 15% missing data and all 46 days with $<$ 50% missing data from 2012. Good results have been attained using the blue-green spectrum, with velocities derived from nLw_490 giving the lowest RMS compared to the HF radar velocities, and correlation values of 0.72 for both u and v. This shows that the method can cope with areas of missing data and that geostationary ocean color satellites do offer a strong case for ocean surface velocity observations. The methodology has been applied to derive novel measurements of the eddy rotation and tidal currents in this region.

In conclusion, the presented method may be suitable for a routinely operated global scheme for deriving low precision velocity fields but may suffer when there is a large level of cloud cover, sunglint, low light or other reasons for reduced data quality. It is expected that if the spatial resolution of the data is improved (e.g., in future satellite missions) then the precision of the method will improve, and lower time separations can be used to derive smaller magnitude velocities.

References

Bian, C., W. Jiang, and R. J. Greatbatch (2013), An exploratory model study of sediment transport sources and deposits in the Bohai Sea, Yellow Sea, and East China Sea, *J. Geophys. Res. Oceans*, *118*, 5908–5923, doi:10.1002/2013JC009116.

Bowen, M. M., W. J. Emery, J. L. Wilkin, P. C. Tildesley, I. J. Barton, and R. Knewtson (2002), Extracting multiyear surface currents from sequential thermal imagery using the maximum cross-correlation technique, *J. Atmos. Oceanic Technol.*, *19*, 1665–1666, doi:10.1175/1520-0426(2002)019$<$1665:EMSCFS$>$2.0.CO;2.

Chapman, R. D., L. K. Shay, H. C. Graber, J. B. Edson, A. Karachintsev, C. L. Trump, and D. B. Ross (1997), On the accuracy of HF radar surface current measurements: Intercomparisons with ship-based sensors, *J. Geophys. Res.*, *102*(C8), 18,737–18,748, doi:10.1029/97JC00049.

Chevallier, C., S. Herbette, L. Marié, P. Le Borgne, A. Marsouin, S. Péré, B. Levier, and C. Reason (2014), Observations of the Ushant front displacements with MSG/SEVIRI derived sea surface temperature data, *Remote Sens. Environ.*, *146*, 3–10, doi:10.1016/j.rse.2013.07.038.

Choi, J.-K., H. Yang, H.-J. Han, J.-H. Ryu, and Y.-J. Park (2013), Quantitative estimation of suspended sediment movements in coastal region using GOCI, *J. Coastal Res.*, *65*, 1367–1372.

Crocker, R. I., D. K. Matthews, W. J. Emery, and D. G. Baldwin (2007), Computing coastal ocean surface currents from infrared and ocean colour satellite imagery, *IEEE Trans. Geosci. Remote Sens.*, *45*(2), 435–446, doi:10.1109/TGRS.2006.883461.

Crout, R. L. (2008), Oil and gas platform ocean current profile data, paper presented at OCEANS 2008, Quebec City, QC, 1–9 pp., 15–18 Sept., doi:10.1109/oceans.2008.5152027.

Emery, W. J., A. C. Thomas, M. J. Collins, W. R. Crawford, and D. L. Mackas (1986), An objective method for computing advective surface velocities from sequential infrared satellite images, *J. Geophys. Res.*, *91*(C11), 12,865–12,878.

Faure, F., P. Coste, and G. Kang (2008), The GOCI instrument on COMS mission – The first geostationary ocean color imager, in *Proceedings of the International Conference on Space Optics (ICSO)*, vol. 6, Toulouse, France, 1–6 pp., 14-17-Oct. [Available at http://www.icsoproceedings.org/.]

Gao, F., L. Qiao, and G. Li (2016), Modelling the dispersal and depositional processes of the suspended sediment in the central South Yellow Sea during the winter, *Geol. J.*, *51*(S1), 35–48, doi:10.1002/gj.2827.

Hu, C., L. Feng, and Z. Lee (2012), Evaluation of GOCI sensitivity for At-Sensor radiance and GDPS-Retrieved chlorophyll-a products, *Ocean Sci. J.*, *47*(3), 279–285, doi:10.1007/s12601-012-0028-0.

Hu, Z., D.-P. Wang, D. Pan, X. He, Y. Miyazawa, Y. Bai, D. Wang, and F. Gong (2016), Mapping surface tidal currents and Changjiang plume in the East China Sea from Geostationary Ocean Color Imager, *J. Geophys. Res. Oceans*, *121*, 1563–1572, doi:10.1002/2015JC011469.

IOCCG (2012), Ocean-colour observations from a geostationary orbit, in *Reports of the International Ocean-Colour Coordinating Group*, edited by D. Antoine, IOCCG, Dartmouth, Canada.

Ito, M., A. Morimoto, T. Watanabe, O. Katoh, and T. Takikawa (2014), Tsushima Warm Current paths in the southwestern part of the Japan Sea, *Prog. Oceanogr.*, *121*, 83–93, doi:10.1016/j.pocean.2013.10.007.

Kamachi, M. (1989), Advective surface velocities derived from sequential images for rotational flow field: Limitations and applications of maximum cross-correlation method with rotational registration, *J. Geophys. Res.*, *94*(C12), 18,227–18,233, doi:10.1029/JC094iC12p18227.

Kim, D.-W., Y.-H. Jo, J.-K. Choi, J.-G. Choi, and H. Bi (2016), Physical processes leading to the development of an anomalously large Cochlodinium polykrikoides bloom in the East sea/Japan sea, *Harmful Algae*, *55*, 250–258, doi:10.1016/j.hal.2016.03.019.

Klemas, V. (2012), Remote sensing of coastal and ocean currents: An overview, *J. Coastal Res.*, *28*(3), 576–586, doi:10.2112/jcoastres-d-11-00197.1.

Matthews, D. K., and W. J. Emery (2009), Velocity observations of the California Current derived from satellite imagery, *J. Geophys. Res.*, *114*, doi:10.1029/2008JC005029.

Oh, E., J. Hong, S.-W. Kim, S. Cho, and J.-H. Ryu (2012), Stray light analysis of nearby slot source using integrated ray tracing technique, in *Sensors, Systems, and Next-Generation Satellites XVI, Proceedings of the SPIE*, *8533*, edited by R. Meynart, S. P. Neeck, and H. Shimoda, 10 pp., SPIE, Edinburgh, doi:10.1117/12.974455.

Padfield, D. (2012), Masked object registration in the fourier domain, *IEEE Trans. Image Process.*, *21*(5), 2706–2718, doi:10.1109/tip.2011.2181402.

Ronen, D. (2011), The effect of oil price on containership speed and fleet size, *J. Oper. Res. Soc.*, *62*(1), 211–216.

Shutler, J. D., et al. (2016), Progress in satellite remote sensing for studying physical processes at the ocean surface and its borders with the atmosphere and sea-ice, *Prog. Phys. Geogr.*, *40*(2), 215–246, doi:10.1177/0309133316638957.

Takikawa, T., J.-H. Yoon, and K.-D. Cho (2003), Tidal currents in the Tsushima Straits estimated from ADCP data by ferryboat, *J. Oceanogr.*, *59*(1), 37–47, doi:10.1023/a:1022864306103.

Takikawa, T., J.-H. Yoon, and K.-D. Cho (2005), The Tsushima Warm Current through Tsushima Straits Estimated from Ferryboat ADCP Data, *J. Phys. Oceanogr.*, *35*(6), 1154–1168, doi:10.1175/jpo2742.1.

Takikawa, T., G. Onitsuka, K.-i. Fukudome, J.-H. Yoon, A. Morimoto, M. Moku, and A. Watanabe (2011), Spatial and temporal variation of a cyclonic eddy detected downstream of the Tsushima Islands in November 2007, *Estuaries Coasts*, *34*(4), 775–784, doi:10.1007/s12237-011-9395-5.

Tokmakian, R., P. T. Strub, and J. McClean-Padman (1990), Evaluation of the maximum cross-correlation method of estimating sea surface velocities from sequential satellite images, *J. Atmos. Oceanic Technol.*, *7*, 852–865.

Wang, M., J.-H. Ahn, L. Jiang, W. Shi, S. Son, Y.-J. Park, and J.-H. Ryu (2013), Ocean color products from the Korean Geostationary Ocean Color Imager (GOCI), *Opt. Express*, *21*(3), 3835–3849, doi:10.1364/oe.21.003835.

Yang, C.-S., and J.-H. Song (2012), Geometric performance evaluation of the Geostationary Ocean Color Imager, *Ocean Sci. J.*, *47*(3), 235–246, doi:10.1007/s12601-012-0025-3.

Yang, H., J.-K. Choi, Y.-J. Park, H.-J. Han, and J.-H. Ryu (2014), Application of the Geostationary Ocean Color Imager (GOCI) to estimates of ocean surface currents, *J. Geophys. Res. Oceans*, *119*, 3988–4000, doi:10.1002/2014JC009981.

Yang, S. Y., H. S. Jung, D. I. Lim, and C. X. Li (2003), A review on the provenance discrimination of sediments in the Yellow Sea, *Earth Sci. Rev.*, *63*(1–2), 93–120, doi:10.1016/S0012-8252(03)00033-3.

Yoshikawa, Y., A. Masuda, K. Marubayashi, M. Ishibashi, and A. Okuno (2006), On the accuracy of HF radar measurement in the Tsushima Strait, *J. Geophys. Res.*, *111*, C04009, doi:10.1029/2005JC003232.

Yoshikawa, Y., A. Masuda, K. Marubayashi, and M. Ishibashi (2010), Seasonal variations of the surface currents in the Tsushima Strait, *J. Oceanogr.*, *66*(2), 223–232, doi:10.1007/s10872-010-0020-1.